Interplay of Support Chemistry and Reaction Conditions on Copper Catalyzed Methanol Steam Reforming

Manuel Antonio Díaz-Pérez,[†] Javier Moya,[†] Juan Carlos Serrano-Ruiz,[†,‡] and Jimmy Faria*[,†,§]

[†]Abengoa Research, C/Energía Solar 1, Campus Palmas Altas, Sevilla, 41014, Spain
[‡]Universidad de Loyola, Andalucía, Department of Engineering, C/Energía Solar 1, Campus Palmas Altas, Sevilla, 41014, Spain
[§]Chemical Processes and Materials, Faculty of Science and Technology, University of Twente, Enschede, The Netherlands
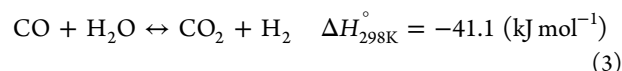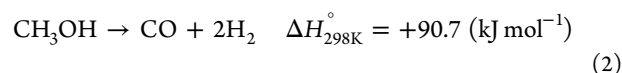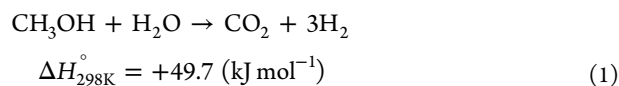
S *Supporting Information*

ABSTRACT: A series of Cu catalysts supported on SiO_2, Al_2O_3−SiO_2, TiO_2 rutile, and Cu/TiO_2 anatase metal oxides has been studied for methanol reforming in the vapor phase. The highest activity was obtained on Cu/SiO_2 catalysts (5493 μmol H_2 min^{-1}·g$_{cat}^{-1}$) followed by Cu/TiO_2 rutile, Cu/Al_2O_3−SiO_2, and anatase. XRD and HRTEM characterization after reaction revealed that on Cu/SiO_2 significant sintering occurred during reaction. In contrast, the particle size growth on Cu/TiO_2 rutile and anatase was less pronounced, which could be associated with the interaction between Cu clusters and TiO_2. Characterization by TGA showed that on Cu/Al_2O_3−SiO_2 the main cause of deactivation was coke deposition.
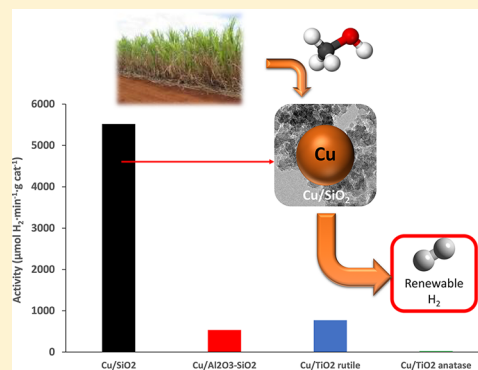
1. INTRODUCTION

Industrial production of hydrogen is accomplished via steam reforming of natural gas or light oil fractions. However, the utilization of fossil-derived feeds hinders its long-term application due to the concomitant greenhouse emissions and environmental pollution. Over the past decade, significant efforts have been made to accelerate the transition to more sustainable hydrogen sources (e.g., bioethanol, biomethanol, biodiesel, and H_2O).[1] In particular, steam reforming of methanol (see reaction 1) offers several advantages when compared to reforming of other renewable feedstocks. Methanol is one of the most efficient energy carriers due to its high molecular H/C ratio (four hydrogen atoms per carbon). Unlike ethanol, the absence of recalcitrant C−C bonds favors the reforming process at low temperatures (240−260 °C), reducing the risk of coke formation typically observed in ethanol reforming (350−800 °C). At the same time, operation at lower temperatures reduces the CO formation since methanol thermal decomposition (see reaction 2) is inhibited at low temperatures. Additionally, utilization of low temperatures is beneficial for the water−gas shift reaction (WGS; see reaction 3), which leads to low levels of CO in the reformate stream.[2] As a result, it is possible to avoid the use of specialized materials in the reactor construction, lowering the overall cost of the system.[3] Finally, operating at relatively mild conditions minimizes undesired surface reconstruction and particle sintering during reaction.[4]

$$CH_3OH + H_2O \rightarrow CO_2 + 3H_2$$
$$\Delta H_{298K}^{\circ} = +49.7 \text{ (kJ mol}^{-1}) \tag{1}$$

$$CH_3OH \rightarrow CO + 2H_2 \quad \Delta H_{298K}^{\circ} = +90.7 \text{ (kJ mol}^{-1}) \tag{2}$$

$$CO + H_2O \leftrightarrow CO_2 + H_2 \quad \Delta H_{298K}^{\circ} = -41.1 \text{ (kJ mol}^{-1}) \tag{3}$$

Copper supported on ZnO/Al_2O_3 oxides is the most commonly used catalyst for methanol steam reforming due to its high activity at low temperatures and high selectivity to H_2.[5,6,15−24,7,25,8−14] In this catalyst, oxygenated molecules bind with the "ideal" strength and configuration to metallic Cu, which facilitates the activation of water molecules and methanol on the surface to produce carboxyl- and carbonyl-containing species that can easily undergo decomposition to CO_2 and H_2.[11,13,26,27] This results in high selectivity to the reforming products (i.e., CO_2 and H_2) and very low decarbonylation and methanation byproducts (i.e., CO and CH_4).[4] For this reason, Cu catalysts have been the subject of extensive research using partially reducible metal oxides (e.g., CeO_2 and TiO_2)[4,5,34−40,6,19,28−33] and nonreducible metal oxides (e.g., SiO_2, Al_2O_3) as catalyst supports.[4,5,34,6,19,28−33]

Recently, it has been shown that Cu/ZnO-Al_2O_3 is an extremely dynamic catalytic system under industrial reaction conditions as evidenced by in situ and ex situ characterization using bulk, surface sensitive, and imaging methods.[41] These catalysts undergo significant structural changes that drastically

affect the selectivity, activity, and ultimately stability of the Cu catalysts.[42] Therefore, understanding the nature of the interactions between Cu clusters and metal oxides is of primary interest to successfully design new catalytic materials with improved catalytic activity, selectivity, and stability. For this reason, in this study, we decided to evaluate the performance of a copper catalyst supported on metal oxides with different surface reducibility, acidity, topology, and crystalline structure to establish activity−structure relationships. For this purpose, we synthesized, characterized, and tested a set of Cu catalysts supported on nanosized SiO_2, Al_2O_3−SiO_2, TiO_2 rutile, and TiO_2 anatase for methanol steam reforming. In addition, the effect of pressure was investigated for the most active catalyst (Cu/SiO_2). At high pressures, it will be possible to directly connect the reactor effluent to a membrane separation unit, decreasing the associated capital and operational costs as the membrane footprint will be substantially reduced.[43] This high-purity hydrogen can be fed to a refuelling station at higher pressures, reducing the number of compression stages required to reach the 600 bar of pressure required in mobility applications.[44,45]

2. EXPERIMENTAL SECTION

2.1. Materials. The methanol used in the reaction was Chromasolv HPLC grade purchased from Sigma-Aldrich with a purity above 99.9%. Copper(II) nitrate trihydrate used as a precursor was also obtained from Sigma-Aldrich (purity ≥99%). The four supports used and their descriptions can be found in Table 1.

Table 1. Description and Physical Properties of the Supports Employed for Catalyst Synthesis

support	description	supplier	BET surface area $(m^2 \ g^{-1})$
SiO_2	Aerosil 380	Evonik	350−410
Al_2O_3−SiO_2 (70%/30%)	Siral 40 HPV	Sasol	500
TiO_2 (100% rutile)		Sigma-Aldrich	50
TiO_2 (100% anatase)	Crystal Activ G5	Crystal France SAS	370

2.2. Catalyst Synthesis. Four different supports were selected to study the performance of copper based catalysts on the methanol steam reforming reaction in the vapor phase. The catalysts studied were prepared by wet impregnation using copper(II) nitrate tryhidrate as a precursor with a loading of 20 wt %. The salt was dissolved using DI water, and the support was added while the solution was stirred (500 rpm). The dispersion was stirred for 48 h at room temperature before evaporating the solvent at 110 °C, maintaining continuous stirring (200 rpm). After this step, the solid was dried at 100 °C overnight. Once the powder was completely dried, it was calcined at 600 °C over 4 h (10 °C min^{-1}).

2.3. Catalyst Characterization. The catalysts were characterized by temperature-programmed reduction (TPR), temperature-programmed desorption of NH_3 (NH_3-TPD), N_2-physisorption, thermal gravimetric analysis (TGA), X-ray diffraction (XRD), and transmission electron microscopy (TEM). TPR characterization of 30 mg of catalyst was performed on a Micromeritics Autochem II 2920 using a gas mixture of 10% H_2 in Ar at a flow rate of 50 mL min^{-1} with a linear heating rate of 5 °C min^{-1} up to 900 °C and holding time of 1 min. H_2 consumption was determined by a thermal

conductivity detector. NH_3-TPD was measured using Micromeritics Autochem II 2920 employing a gas mixture of 15 vol % NH_3/He. The surface was initially cleaned with He, then it was reduced in 50 sccm of H_2/Ar 10/90 vol % at 230 °C for 3 h to replicate the reduction conditions employed during the catalyst activation. Then, the system was purged with He at 230 °C to remove any water formed. Once the temperature reached 35 °C, 15% NH_3/He was passed through the sample for 60 min. Finally, a temperature ramp of 10 °C min^{-1} up to 900 °C was employed to study the desorption profile. Total acidity of the catalysts was determined by integrating the area under the curve of the NH_3-TPD. The desorption was measured by thermal conductivity detector (TCD). Nitrogen adsorption isotherms were obtained using a Micromeritics ASAP 2020. The data were fitted using Brunauer−Emmett−Teller (BET) theory to calculate surface area and porous size distribution. The physisorption of nitrogen was performed at liquid nitrogen temperature (77 K), and the degasification step was carried out at 200 °C over 4 h. Prior to analysis, the samples were degassed in situ at 230 °C for 24 h. The micropore volume was derived from the t-plot method (relative pressure range: 0.2−0.6), and the total pore volume was determined at p/p_0 = 0.99. Surface areas were measured before and after reaction. The crystallinity of the sample and the identification of the crystalline species were determined using a D8I Bruker XRD for powder samples with incident slits and with a Cu anode working at 40 kV and 40 mA. The data were collected in an angle range from 30 to 60°. A semiquantitative method was used to determine the crystalline structure by comparison to the database of Joint Committee on Powder Diffraction Standards (JCPDS). The average size of the crystallites was calculated using the Debye−Scherrer eq (eq 4).

$$\tau = \frac{0.9 \times \lambda}{\beta \times \cos \theta} \tag{4}$$

For the HRTEM characterization, a Philips CM200 microscope (200 kV) with a structural resolution of 0.14 nm between lines and 0.23 nm between points equipped with X-ray Energy Dispersive Analyzer (EDX X-Max 80T, Oxford Instruments) and a CCD GATAN camera for image acquisitions was employed to characterize the nanostructure of the catalysts. Each sample was prepared by sonicating the powder in n-butanol to improve the dispersion of the particles. The catalyst particles were dropwise transferred to a holey carbon coated 300 mesh copper grid. The catalysts were characterized before and after reaction. TGA experiments were performed in a TA Instruments SDT Q-600 thermobalance. The TGA analyses were performed using high purity air to measure the amount of carbon deposited on the catalyst. The first step consists of an increasing temperature ramp from 25 to 110 °C at a rate of 5 °C min^{-1}. Once 110 °C is reached, the temperature is maintained for 20 min before carrying out a quenching to 40 °C. Then, the temperature is increased to 550 °C at a ramp of 10 °C min^{-1}. Finally, 550 °C is maintained over 60 min.

2.4. Reaction System. The catalytic activity and selectivity of the different catalysts were measured in the vapor phase using an automated Microactivity Effi reactor from PID at low and high pressures. The methanol/water mixture was fed by an HPLC pump and evaporated at 180 °C. The steam to methanol ratio was 1:1.5. The vapor stream entered the reactor and passed through the catalyst bed placed inside a tubular

reactor made of stainless steel 310 at the desired reaction temperature and pressure. Once steady state conditions were achieved, the product stream was sent to a condenser where the unreacted methanol and water were eliminated. The reforming stream was continuously analyzed by gas chromatography. The analysis of the liquid phase allowed the quantification of the conversion, and undesired condensable products formed. The conversion was calculated in terms of methanol consumed, and the selectivity was determined considering the products obtained through the reaction, i.e., S_{H_2} = mol min^{-1} H$_2$/(mol min^{-1} H$_2$ + mol min^{-1} CO$_2$ + mol min^{-1} CO); S_{CO} = mol min^{-1} CO/(mol min^{-1} H$_2$ + mol min^{-1} CO$_2$ + mol min^{-1} CO). The carbon mass balance in all the experiments was above ~95%.

3. RESULTS AND DISCUSSION

3.1. Steam Reforming of Methanol on Cu Catalysts.
3.1.1. Effect of the Catalyst Support. The catalysts were tested for the methanol steam reforming reaction at 280 °C using a continuous flow reactor for at least 4 h (Figure 1). The
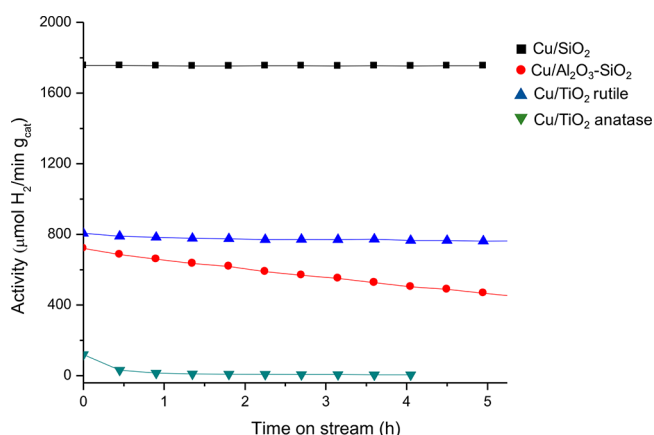

Figure 1. Catalytic activity as a function of time on stream of the different catalysts: Cu/SiO$_2$ (■), Cu/Al$_2$O$_3$−SiO$_2$ (●), Cu/TiO$_2$ rutile (▲), and Cu/TiO$_2$ anatase (▼) during steam reforming of methanol at atmospheric pressure and 280 °C and a steam to methanol ratio of 1:1.5.

catalytic activity and stability of these materials measured in terms of hydrogen production varied significantly depending on the support employed. For instance, on Cu/SiO$_2$ the catalytic activity was significantly higher than the rest of the catalysts with values around 1750 μmol H$_2$ min^{-1} g$_{cat}$$^{-1}$ at 80% methanol conversion. While this value was significantly higher than those observed on Cu supported on Al$_2$O$_3$, TiO$_2$ rutile, and TiO$_2$ anatase, the level of conversion was close to the equilibrium (>99%). Therefore, Cu-SiO$_2$ true catalytic activity cannot be determined under these conditions. To properly address this issue, additional experiments were performed at lower conversion (60%), and the activity under steady state conditions was ~5500 μmol H$_2$ min^{-1} g$_{cat}$$^{-1}$ (see Table S1). Notably, in the case of Al$_2$O$_3$−SiO$_2$, the hydrogen production rate started at ~700 μmol H$_2$ min^{-1} g$_{cat}$$^{-1}$ and progressively decreased to ~500 μmol H$_2$ min^{-1} g$_{cat}$$^{-1}$ after 5 h of reaction. Cu/TiO$_2$ rutile showed higher productivities than Cu/Al$_2$O$_3$−SiO$_2$ with values of ~800 μmol H$_2$ min^{-1} g$_{cat}$$^{-1}$.

In terms of stability, Cu/TiO$_2$ rutile retained its catalytic activity throughout the 5 h of reaction. In contrast, Cu/TiO$_2$ anatase showed significant rates of deactivation and low H$_2$ productivity. At the beginning of the reaction, the activity was 180 μmol H$_2$ min^{-1} g$_{cat}$$^{-1}$, and after 4 h of reaction this value decreased to 21.8 μmol H$_2$ min^{-1} g$_{cat}$$^{-1}$. As a result, the catalytic activity of the Cu catalysts followed the following trend SiO$_2$ > TiO$_2$ rutile > Al$_2$O$_3$−SiO$_2$ > TiO$_2$ anatase. Furthermore, assessment of the internal mass transport limitations using the Weisz−Prater criterion showed that these catalysts are not affected by intraparticle diffusion limitations (see Table S2).

The average product distribution obtained during the 4−5 h reaction (Figure 2a) indicated that on Cu catalysts the formation of light hydrocarbons (methane, ethane, ethylene) was undetectable using GC-FID/TCD; except on TiO$_2$ anatase, small quantities of CH$_4$ were observed (0.04 mol % in wet basis). Furthermore, analyses of the liquid condensate collected after the microreactor step indicated that no oxygenated species were formed during reaction. On Cu/SiO$_2$ and Cu/TiO$_2$ rutile catalysts, the CO concentration was significantly higher (~0.35 and 0.2 mol %, respectively), while in the case of Cu/Al$_2$O$_3$−SiO$_2$ and Cu/TiO$_2$ anatase only ~0.05 mol % was detected (Figure 2b).
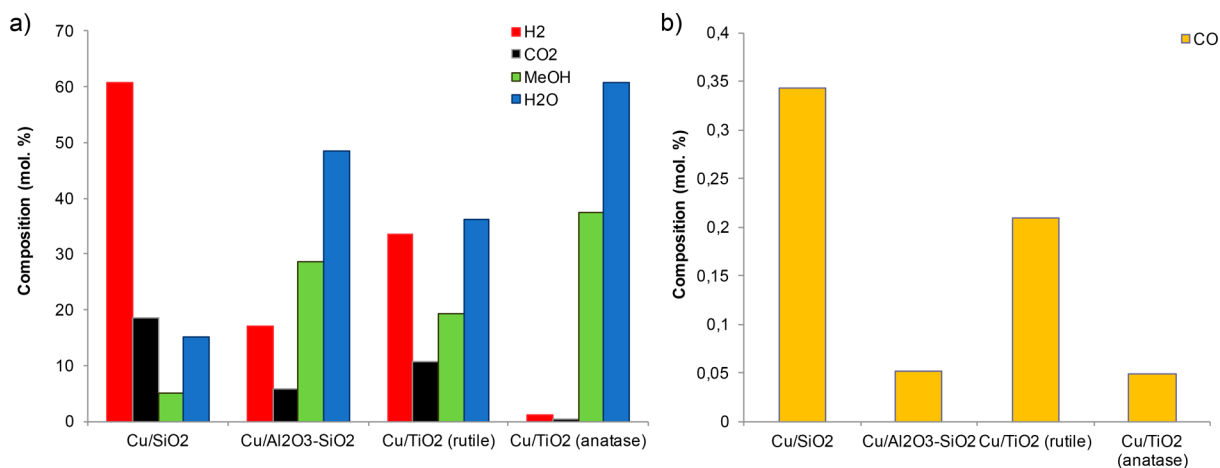

Figure 2. Product distribution (a) and carbon monoxide composition (b) on a wet basis obtained after 4 h of methanol steam reforming at atmospheric pressure and 280 °C for Cu/SiO$_2$, Cu/Al$_2$O$_3$−SiO$_2$, Cu/TiO$_2$ rutile, and Cu/TiO$_2$ anatase at a W/F of 1200 kg/L h^{-1}.

In terms of selectivity, however, Cu/TiO_2 anatase showed the highest CO and CH_4 selectivity with values of 2.3 and 2%, respectively (see Table S3). In contrast, Cu supported on SiO_2, $Al_2O_3-SiO_2$, and TiO_2 rutile resulted in CO selectivity below 0.5% and negligible CH_4 amounts at similar levels of conversion. The ratio of CO_2 to CO and H_2 to CO_2 are good indicators of the contributions of the methanol reforming reaction, methanol decomposition, and coke formation.[3,4] For instance, on Cu supported on SiO_2, $Al_2O_3-SiO_2$, and TiO_2 rutile, similar ratios of H_2/CO_2 were obtained with values ranging from 3.1 to 3.3. In contrast, Cu/TiO_2 anatase showed a H_2/CO_2 ratio above 3.5. The higher ratio of hydrogen to carbon dioxide on Cu/TiO_2 anatase could be associated with higher rates of methanol decomposition or other parallel pathways that can generate hydrogen (e.g., coke deposition and dehydrogenation). At the same time, the CO_2/CO ratio value was 7.40, which is significantly lower than that obtained on SiO_2 (231), $Al_2O_3-SiO_2$ (87), and TiO_2 rutile (47) catalysts. The low catalytic activity and poor stability and selectivity of Cu/TiO_2 anatase compared to rutile could be associated with the differences in the Lewis acidity of partially uncoordinated Ti^{4+} cations, which in turn affects the interaction of polar molecules with the surface.[46−48]

3.1.2. Effect of W/F, Temperature, and Pressure on Cu/SiO_2 Performance. To further explore the stability, selectivity, and activity of the Cu/SiO_2 catalyst, we decided to investigate the product distribution as a function of the catalyst to feed ratio and time on stream (TOS) at low and high temperatures (260−280 °C) and pressures (1 and 25 bar). As shown in Figure 3, increasing temperature enhanced the activity; however, as the conversion approached the equilibrium (∼90%), this effect was attenuated. Notably, the ratio of H_2 to CO_2 increased from 3.32 to 3.64 when the temperature was increased from 260 to 300 °C. The opposite trend was observed on the CO to CO_2 ratio (see Table S4). This ratio drastically decreased from 153 to 45 with temperature. These trends could be attributed to a combination of different factors, including (1) changes in the relative kinetics of methanol decomposition (reaction 2) and reforming reaction (reaction 1), (2) differences in surface coverage as the conversion increases, and (3) surface reconstruction accompanied by Cu sintering.[26] Due to the high conversions reached under these reaction conditions, it was not possible to assess the activation energies. This issue will be addressed in future studies in our group.

The stability of the catalyst was studied under four different reaction conditions over the course of ∼20 h, in which catalyst-to-feed ratio (W/F) was varied from 300 to 600 kg/(L s⁻¹) at reaction temperatures ranging from 260 to 300 °C and atmospheric pressure (Figure S1). Initially, the catalyst was operated at an intermediate W/F of 300 kg/(L s⁻¹) and 260 °C for 4 h reaching a conversion of 56% and high selectivity for CO_2 and H_2 with no apparent changes over the course of the reaction. The catalyst showed no sign of deactivation even at high temperatures. Further studies at high and low pressures were performed to determine the stability of the catalyst and selectivity under harsh reaction environments. The results showed that in the case Cu/SiO_2 the conversion and product distributions remained constant over the TOS explored at low and high pressures (Figure 4). However, the conversion and products concentration at high pressure were reduced compared to those obtained at low pressure. This change in activity was accompanied by a change in selectivity. The CO
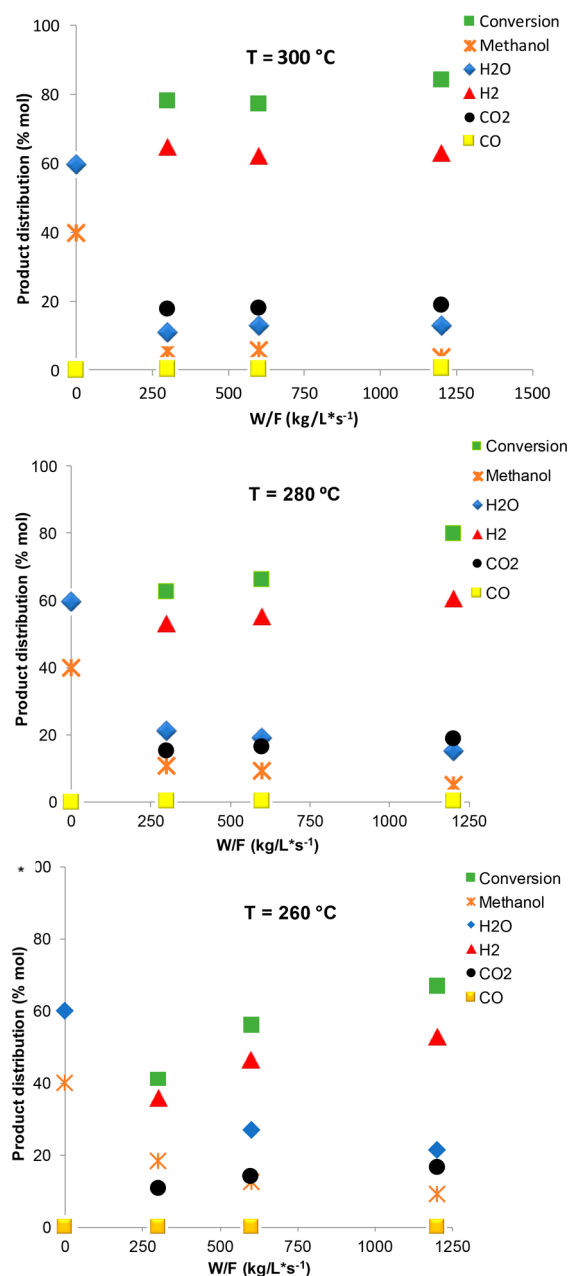

Figure 3. Product distribution on a wet basis as a function of W/F obtained during methanol steam reforming at atmospheric pressure on Cu/SiO_2 at different W/F (300−1200 kg of catalyst/L·s⁻¹) and temperatures (260−300 °C).

concentration was 0.3 mol % at low pressures (TOS ranging 10 to 80 h), while in the high pressure tests this value was nearly 3-fold higher (∼0.9 mol %). One could imagine that as pressure increases, capillary condensation inside the porous structure of the catalyst is favored.[49] The liquid layer could create additional limitations to the mass transport of molecules or solvate kinetically relevant reaction intermediates.[50−53] In turn, the reaction kinetics are attenuated. In addition, it could be possible that upon formation of liquid inside the porous structure, the Cu catalyst surface is modified or reconstructed, hindering the formation of the surface formate (−HCOOH) via $\eta^1(O)$-binding, which is believed to be the precursor of CO_2 and hydrogen in methanol reforming on oxophilic catalytic surfaces (e.g., Cu).
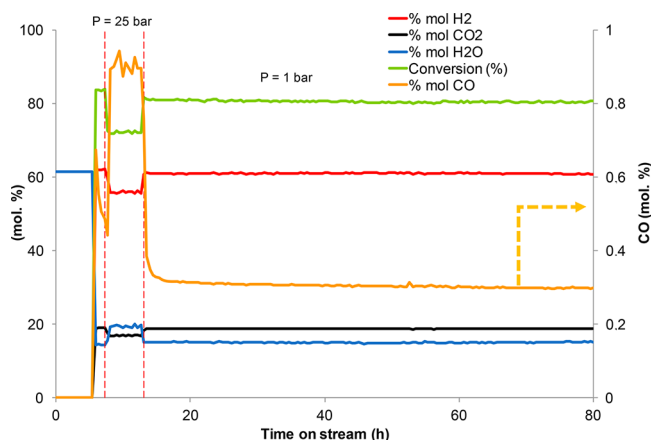
Figure 4. Product distribution on a wet basis as a function of time on stream (TOS) obtained during methanol steam reforming at atmospheric pressure and 25 bar at 280 °C on Cu/SiO_2 at different W/F (1200 kg of catalyst/L h^{-1}).

Here, it is important to remember that at high conversions it is not possible to determine the stability of a catalyst solely based on the TOS profile as an excess of catalyst will mask the deactivation. For this reason, postreaction characterization was performed to determine the extent of catalyst sintering and coke deposition (see section 3.2).

3.2. Catalysts Characterization. *3.2.1. Reducibility and Acidity.* To interpret the differences in activity and selectivity observed, we decided to characterize the reducibility and acidity of these catalysts by temperature-programmed reduction (TPR) and temperature-programmed desorption of ammonia (TPD-NH_3). As shown in Figure 5, SiO_2 and Al_2O_3–SiO_2 showed a symmetric peak centered at 275 and 256 °C, respectively (see Figure 5a,b). This reduction peak was assigned to the reduction of Cu^{2+} to Cu^0.[26] In contrast, a more complex fingerprint of Cu reduction was observed on TiO_2 rutile and anatase (Figure 5c,d). The Cu supported on a TiO_2 rutile catalyst was reduced between 90 and 215 °C with a maximum at 184 °C, while on TiO_2 anatase, the Cu reduction started at higher temperatures (~120 °C) with its maximum centered at 193 °C. As shown in Table S5, the extent of reduction for the four catalysts was similar (90 to 98%), indicating that reduction can be accomplished at lower temperatures than those reported for bulk Cu (350–500 °C).[28]

To further understand the differences between the four catalysts, the TPR profiles were deconvoluted and quantified using a Gaussian fitting model. In Figure 5c,d, the TPR profile was fitted using three Gaussian curves centered at approximately 135, 180, and 195 °C, for Cu on TiO_2 rutile and anatase (distribution plot in Figure S2). The results indicated that on TiO_2 anatase the major contribution to the hydrogen consumption took place at around 195–200 °C, while in the case of TiO_2 rutile the reduction occurred at the lower temperature ranges of 130–135 °C and 180–185 °C (see Figure 5d). The higher reducibility of Cu on TiO_2 rutile and anatase could be attributed to metal–support interactions, which can alter the electronic properties of the Cu surface.[54–56] The lower reduction temperatures of Cu supported on TiO_2 rutile could be attributed to a higher degree of metal dispersion.[57,58] In contrast, on nonreducible metal oxides (e.g., SiO_2 and Al_2O_3–SiO_2), all the Cu clusters
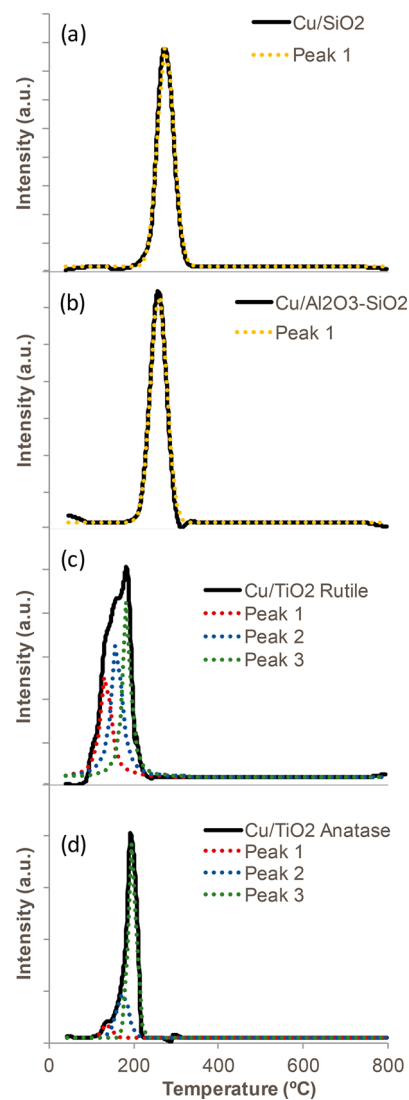

Figure 5. Temperature-programmed reduction of the Cu/SiO_2 (a), Cu/Al_2O_3–SiO_2 (b), Cu/TiO_2 rutile (c), Cu/TiO_2 anatase (d) catalysts.

were reduced at higher temperatures and in a narrow temperature range (260–270 °C).

TPD-NH_3 analyses were performed to measure the catalyst acidity (Figure 6). The desorption of NH_3 on SiO_2 and Al_2O_3–SiO_2 started at mild temperatures (~38 °C) and finished at 340 and 458 °C, respectively. On Cu/SiO_2, two desorption peaks were observed at 70 and 340 °C. In the case of Cu/Al_2O_3–SiO_2, two broad desorption peaks were observed, the first one at 80 °C and the second one at 290 °C. In contrast, in Cu/TiO_2-supported catalysts the amount of NH_3 desorbed was negligible. In the case of Cu/TiO_2 anatase, a broad peak was observed in the low temperature range (68–142 °C). Similarly, on Cu/TiO_2 rutile the desorption extended from 78 to 170 °C. While it is tempting to associate the desorption temperatures to the surface–adsorbate interactions, the studies published by Prof. R. Gorte demonstrated that the possible interference of other phenomena (e.g., mass transport limitations and adsorbate–adsorbate interactions) hinders the utilization of this technique to obtain energetic parameters.[59–62] As a result, it is not possible to obtain valid conclusions regarding strength of the acid sites on the
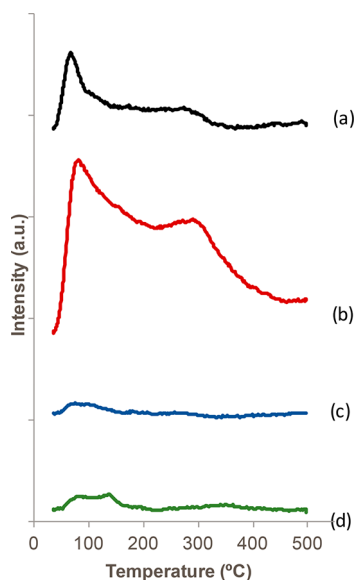
Figure 6. Temperature-programmed desorption of ammonia (TPD-NH$_3$) fingerprints for the Cu/SiO$_2$ (a), Cu/Al$_2$O$_3$−SiO$_2$ (b), Cu/TiO$_2$ rutile (c), Cu/TiO$_2$ anatase (d) catalysts.

materials herein studied. Instead, the total acid site density has been calculated (see Table 2).

Table 2. Acid Site Density of the Different Catalysts Obtained from Temperature Programmed Desorption of Ammonia (NH$_3$-TPD)

catalysts	acid site density (μmol g^{-1})	acid site density (μmol m^{-2})
Cu/SiO$_2$	503.9	2.2
Cu/Al$_2$O$_3$−SiO$_2$	1871.1	6.7
Cu/TiO$_2$ rutile	17.6	1.8
Cu/TiO$_2$ anatase	33.2	3.3

The concentration of acid sites on TiO$_2$ rutile and anatase was rather small. One would expect the metal-TiO$_2$ catalysts to have a higher concentration of acid sites. For instance, Aranda et al.[63] reported that on Ru supported TiO$_2$ catalysts, the surface acid site concentrations varied from 312 to 551 μmol NH$_3$ g$_{cat}$$^{-1}$. However, in that case, the interaction of Ru clusters with the support facilitated the reduction of the Ti^{4+} to Ti^{3+} cations. These oxygen vacancies effectively bound ammonia to the catalyst surface, resulting in a higher surface concentration of acid sites. Similar results have been published by Pham et al. on Ru/TiO$_2$/C for the decarboxylative ketonization of organic acids in the liquid phase.[64] In the case of Cu/TiO$_2$, the extent of support (TiO$_2$) reduction was negligible, as shown by TPR measurements (Table S5), explaining the lower concentration of surface acid sites or Ti$^{\delta+}$ uncoordinated cations. As expected, the highest concentration of acid sites per gram of catalyst was observed on Cu/Al$_2$O$_3$−SiO$_2$. On this catalyst, the primary source of acidity comes from the Si−O−Al bridging sites, where the charge unbalance between Si^{4+} and Al^{3+} creates an acid site. In the dehydrated state, the Al^{3+} cations bonded to three oxygens have an electron-pair vacancy that can be filled by sharing an electron pair with a base, i.e., Lewis acid sites. In the presence of water, the Al cations serve as electron acceptors of one free-electron of oxygen in H$_2$O leaving an ionizable proton available for reaction, i.e., Brønsted acid sites.[65,66] At

the reaction conditions herein employed, the high concentration of vapor water facilitates the formation of Brønsted acid sites on the catalyst surface. These sites can accelerate the formation of unsaturated species that can polymerize on the surface deactivating the Cu clusters, explaining the fast rate of catalyst deactivation observed on Cu/Al$_2$O$_3$−SiO$_2$ catalysts.

Notably, on SiO$_2$, the stability and catalytic activity were not affected by the presence of a small concentration of acid sites. To rationalize these results, it is important to consider the reaction mechanism behind the steam reforming reaction of methanol. Detailed kinetic analysis of methanol steam reforming on Cu, Pd, Pt, Ni, and Rh supported on SiO$_2$ has shown that on Cu surfaces the reaction mechanism is drastically different, when compared to the other metals.[12,13,67] According to Takezawa and Iwasa, the methanol reforming reaction on Cu starts with the dehydrogenation of CH$_3$OH to HCHO. This surface aldehyde is attacked by nucleophilic addition of −OH or H$_2$O to produce a HCOOH species that easily decomposes into CO$_2$ and H$_2$. Surface science studies have shown that aldehydes adsorb on IB metals (e.g., Cu and Ag) preferentially via η^1(O)-structure. In this configuration, the molecular identity of the C−O bond is retained, which facilitates the nucleophilic attack of −OH surface species. This mechanism is very different from that observed on group VIII metals, where η^2(CO) binding is more favorable and decomposition of methanol to CO and H$_2$ is enhanced. Sagar et al.[57] showed that moderate and weak acidic sites of Al$_2$O$_3$−ZrO$_2$ were beneficial for the dehydrogenation of cyclohexanol. One can envision that on Cu/SiO$_2$ the lower concentration and weaker acid sites favored the stability of the catalyst compared to Al$_2$O$_3$−SiO$_2$, where the formation of unsaturated oxygenates accelerated carbon deposition on Cu and pore blockage.

3.3. Assessment of the Catalyst Deactivation. *3.3.1. Thermal Gravimetric Analysis (TGA).* Thermal gravimetric analysis of the catalysts after reaction was performed to determine the concentration and type of carbon deposits after reaction. It is worth mentioning that in the case of Cu/SiO$_2$ the analysis was performed after 20 h of continuous reaction, while the rest of the catalysts were analyzed after 5 h of reaction. As shown in Figure 7, all the samples, except for Cu/Al$_2$O$_3$−SiO$_2$, showed a net growth of mass, which could be a consequence of the oxidation of metallic copper to CuO. This oxidation can be clearly observed in the sample Cu/TiO$_2$ anatase, where a two-step mass growth was evident. The first step was associated with the oxidation from Cu to Cu$_2$O, and the second one was due to the step Cu$_2$O to CuO. The theoretical total mass increase was 5%. This value was reached only in the Cu/TiO$_2$ anatase. Notably, on Cu/SiO$_2$ and Cu/TiO$_2$ rutile mass growth was 4.2% and 2.8%, respectively. The differences between experimental and theoretical mass increase could be caused by diffusional limitations of air inside the catalyst particles, originated by a partial collapse of the support (especially in TiO$_2$ rutile) or due to a simultaneous copper oxidation and coke elimination. The sharp mass loss observed on Cu/SiO$_2$ could be attributed to this process. The presence of carbon residues was more prominent in Cu/Al$_2$O$_3$−SiO$_2$ where the decrease of the mass was constant (∼7%). The carbon content for each sample was estimated assuming that during the TGA analysis (a) all the Cu metal (i.e., 20%) was oxidized to CuO, leading to a theoretical weight gain of 5.03%, and (b) all the carbon deposits were oxidized to CO$_2$ and H$_2$O. The results of this analysis are summarized in Table S6. Here,
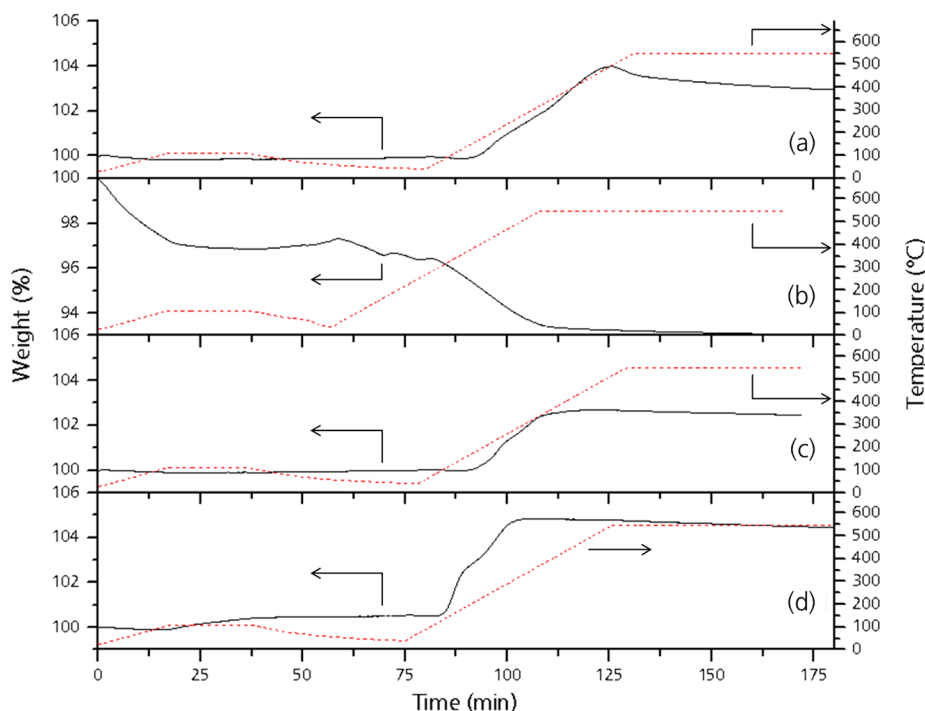
Figure 7. Thermal gravimetric analyses of the different catalysts after 5 h (20 h for Cu/SiO$_2$) of a steam reforming reaction at atmospheric pressure and 280 °C using an aqueous solution of methanol (13.4 M). The samples analyzed were Cu/SiO$_2$ (a), Cu/Al$_2$O$_3$−SiO$_2$ (b), Cu/TiO$_2$ rutile (c), and Cu/TiO$_2$ anatase (d). The weight evolution is presented in a continuous line (left axis) and the temperature in a dashed line (right axis).

it can be noted that carbon content reached the highest value on Cu/Al$_2$O$_3$−SiO$_2$ (∼12%). In this sample, the fast mass losses at the beginning of the experiment could be attributed to the presence of volatile species absorbed and carbon deposits.

In a recent review, it was highlighted that methanol can undergo C−C bond coupling to form unsaturated hydrocarbons (i.e., methanol to olefins) in the presence of acid sites, disproving previous studies that suggested that these C−C couplings during the methanol to olefins process was due to small impurities in the feed.[68] Although the reaction temperatures herein employed are relatively lower than in the case of the methanol to olefins process, the surface reaction intermediates are the same (i.e., surface formate). This intermediate can either decompose to H$_2$ and CO$_2$ on a metallic Cu site[12,13,67] or undergo C−C coupling to form unsaturated hydrocarbons on an acid site. This surface formate is also reported to be responsible for the high selectivity to H$_2$ and CO$_2$ on Cu catalysts.[68] Thus, it is possible that the higher acidity of the Cu/Al$_2$O$_3$−SiO$_2$ catalyst is responsible for the fast rates of deactivation and large carbon deposits (see Table S7). In contrast, on Cu/SiO$_2$ the acid sites did not activate C−C coupling reactions. This is even more relevant if one considers that, in the case of Cu supported on SiO$_2$, the reaction experiments were performed for 20 h and temperatures ranging from 260 to 300 °C.

3.3.2. Textural and Microstructure Characterization (N$_2$ Physisorption, XRD, HR-TEM). Detailed characterization by N$_2$ physisorption, XRD, and HRTEM was performed to further understand the differences in catalytic activity and stability for the methanol steam reforming reaction. As shown in Figure S4a, all the samples showed a type IV adsorption curve. Cu/SiO$_2$ and Cu/Al$_2$O$_3$−SiO$_2$ showed the presence of desorption hysteresis caused by the presence of meso-porosity in the system. In contrast, in the Cu/TiO$_2$ anatase and rutile

catalysts, the hysteresis process is less pronounced. As shown by BJH analysis of the data (Figure S4b), all the materials were meso- and macroporous. In the case of the Cu/SiO$_2$ catalyst, the pore size distribution was narrower, and the maximum of the distribution was centered at ∼320 Å. In contrast, on Cu/Al$_2$O$_3$−SiO$_2$ the distribution of pore sizes was wider and centered at ∼71 Å. As a result, the average pore size, determined by Brunauer−Emmett−Teller (BET) theory, was larger on Cu/SiO$_2$ (see Table 3). On TiO$_2$ rutile and anatase, the pore size distributions were wider, and the maxima of the peaks were centered at ∼400 and ∼700 Å, respectively.

Table 3. Surface Area, Micro- and Mesoporous Area, Ratio Meso- to Microporous Area, and Average Pore Size of Cu/SiO$_2$, Cu/Al$_2$O$_3$−SiO$_2$, Cu/TiO$_2$ Rutile, Cu/TiO$_2$ Anatase before (BR) and after Reaction (AR)

catalysts		surface area (m^2 g^{-1})	microporous area (m^2 g^{-1})	mesoporous area (^{2} g^{-1})	average pore size (Å)
Cu/SiO$_2$	BR	228	8	220	188
	AR	223	1	222	195
Cu/SiO$_2$−Al$_2$O$_3$	BR	279	21	258	115
	AR	214	7	207	124
Cu/TiO$_2$ (rutile)	BR	10	0.8	9	138
	AR	11	0.9	10	155
Cu/TiO$_2$ (anatase)	BR	10	1.1	9	233
	AR	16	0.5	15	219

Notably, after reaction the relative saturation pressure for all the catalysts is lower, indicating a decrease in the N$_2$-accessible surface. As shown in Table 3, the changes in surface area of Cu/SiO$_2$ and Cu/Al$_2$O$_3$−SiO$_2$ were more pronounced than those observed on Cu/TiO$_2$ anatase and rutile. The initial surface areas of Cu/SiO$_2$ (228 m^2 g^{-1}) and Cu/Al$_2$O$_3$−SiO$_2$
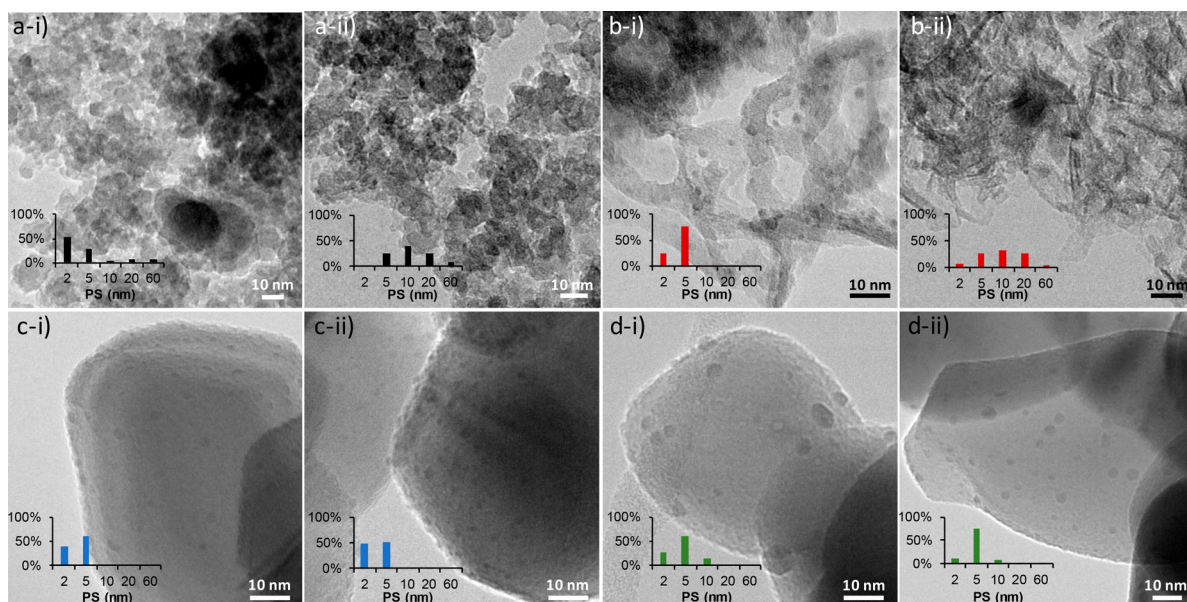
Figure 8. Transmission electron microscopy dark field (TEM-DF) and Cu particle size distribution of the different catalysts (i) before and (ii) after reaction of (a) Cu/SiO$_2$, (b) Cu/Al$_2$O$_3$–SiO$_2$, (c) Cu/TiO$_2$ rutile, and (d) Cu/TiO$_2$ anatase.
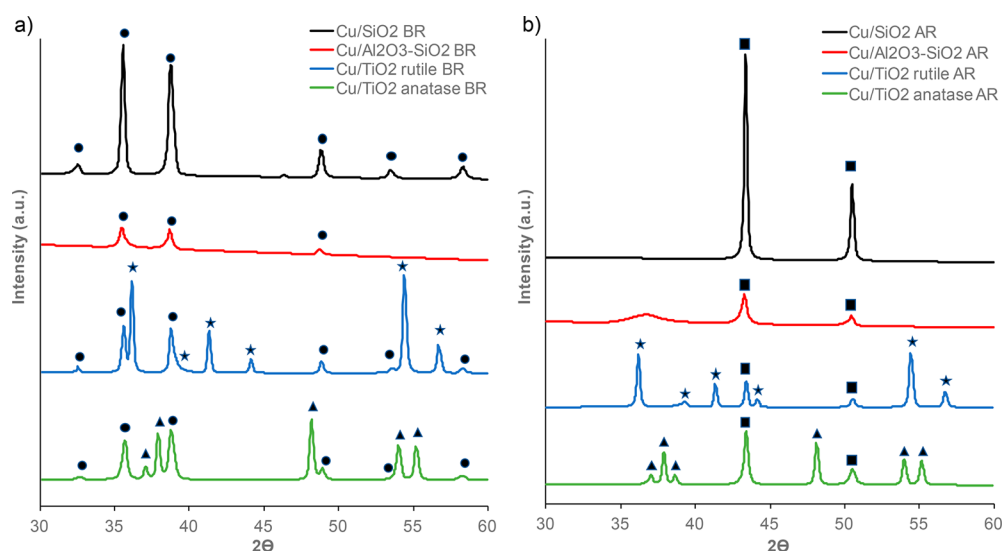

Figure 9. X-ray diffraction of the different catalyst before reaction (a) and after 5 h of reaction (b), except for Cu/SiO$_2$ in which the reaction was performed for 20 h. Depending on the composition of the material, three crystalline phases were detected, including CuO (●), Cu (■), TiO$_2$ rutile (★), and TiO$_2$ anatase (▲).

(279 m^2 g^{-1}) were significantly higher than the homologous catalyst supported on TiO$_2$ anatase and rutile (~10 m^2 g^{-1}). After reaction, the surface area of Cu/TiO$_2$ anatase and rutile slightly increased. This could be due to a reduction of the primary particle size caused by mechanical stress of the catalysts during reaction.[69] The opposite was observed on Cu/Al$_2$O$_3$–SiO$_2$. In this case, a significant reduction of the surface area was observed (~23% decreased). This could be due to a combination of surface reconstruction, pore collapse, or pore blockage.[70] In the case of Cu/SiO$_2$, the decline in surface area was not significant (~2% decreased) even after 20 h of reaction.

To characterize the nanoarchitecture of the Cu catalysts, HR-TEM was performed on the reduced catalysts before and after reaction (see Figure 8). The microscopic structure of nanosized SiO$_2$ and Al$_2$O$_3$–SiO$_2$ catalysts resembled that of

agglomerated nanoparticles, which explains the high surface area and mesoporosity of the materials (>200 m^2 g^{-1}). On TiO$_2$ supports, the primary particles showed needle-like structure. In terms of particle size distribution, SiO$_2$ and Al$_2$O$_3$–SiO$_2$ had particle sizes ranging from 2 to 60 nm, with an average Cu particle size of 4 ± 8 nm and 3 ± 1 nm, respectively. As shown in Figure 8a-i and b-i, the particle size distribution was nearly bimodal on Cu/SiO$_2$ with 75% of the particles in the range of 2 to 5 nm. The rest of the particles were in the range of 10 to 60 nm. In the case of Cu/TiO$_2$ rutile and anatase, the average particle size of Cu nanoparticles was ~3 ± 2 nm. Notably, these results indicate that the catalytic activity observed on Cu supported on SiO$_2$ cannot be entirely explained in terms of metal dispersion as the catalysts with the lowest average particle size (i.e., Cu/TiO$_2$ rutile and anatase) showed lower catalytic activities than those of Cu/SiO$_2$.

After the reaction, the Cu particle size distribution was wider in all of the samples (see Figure 8a-ii to d-ii). The Cu/SiO$_2$ showed the highest degree of sintering after 20 h of reaction at 280 °C with average particle sizes of 9 ± 3 nm. In the case of Cu/Al$_2$O$_3$−SiO$_2$, the particle size after reaction was wider compared to the fresh catalyst, and the average size was 8 ± 3 nm. In contrast, on Cu/TiO$_2$ rutile and anatase, the average particle only slightly increased. These differences could be associated with the metal−support interactions between TiO$_2$ and Cu clusters.[71] For this reason, industrial Cu catalysts use ZnO combined with other metal oxides (e.g., Ce, TiO$_2$, Al$_2$O$_3$) as support. The electronic character of ZnO favors the interaction with Cu, which in turn enhances stability.[9,14,16,28,71−74] It is important to remember that care must be taken in the utilization of HRTEM images as the only tool for the assessment of the catalyst particle size distribution.[75,76] This method is hindered by the small volume of sample analyzed. For this reason, this technique is quite effective when the particle size distribution is narrow, the contrast between the support and metal particles is sufficient (i.e., differences in atomic number are high), the sample-electron beam interaction is not significant, and the sample is homogeneous. Thereby, it is important to combine this technique with complementary characterization (e.g., X-ray diffraction).

XRD characterization of the catalysts was performed to determine the crystalline structure and crystallite size of the Cu species present on the different catalysts before and after the reforming reaction (see Figure 9a). On Cu/SiO$_2$, the intense diffraction peaks at 32, 35.5, 38, 48, 53, and 57° were indexed to the crystalline planes (110), (11$\bar{1}$), (111), (200), (20$\bar{2}$), and (002) of monoclinic tenorite CuO$_2$ (JCPDS 481548).[77,78] In the case of Cu/Al$_2$O$_3$−SiO$_2$, the peak intensity of the diffraction fingerprint of monoclinic CuO significantly decreased, which could be associated with either a smaller particle size of CuO or a lower degree of crystallinity.[79] The absence of diffraction peaks of SiO$_2$ and Al$_2$O$_3$−SiO$_2$ indicated that these high-surface area supports were amorphous. On CuO supported on TiO$_2$, it was possible to identify both CuO monoclinic structure and TiO$_2$ rutile and anatase phases. In the case of Cu/TiO$_2$ rutile, the diffraction peaks 36, 38, 42, 44, 54, and 56° corresponded to the crystalline planes (101), (200), (111), (210), (211), and (220) of TiO$_2$ rutile phase (JCPDS 820514), indicating the high purity of this crystalline material. On Cu/TiO$_2$ anatase, the diffractions at 37.5, 48, 54, and 55° were indexed to the crystalline planes (004), (200), (105), and (211) TiO$_2$ rutile phase (JCPDS 21-1272).[80]

After several hours of reaction, the materials were characterized by XRD to determine the crystalline structure of Cu metal nanoparticles (Figure 9b). In the four catalysts, the absence of CuO monoclinic reflections indicates that reduction of Cu^{2+} to Cu^0 was completed under these conditions. While it is possible that CuO is still present in the system, the fraction of metal oxide ranged between 2 and 10% according to TPR data (Table S5). On Cu/SiO$_2$ and Cu/Al$_2$O$_3$−SiO$_2$, diffractions at 44 and 50° were attributed to the (111) and (200) planes that are characteristic of the faced centered cubic (fcc) structure of metallic Cu with the space group of $Fm3m$ (JCPDS 85-1326).[81] The intensity and broadening of the reflections, however, indicated that on SiO$_2$ the particles were more crystalline and larger compared to Al$_2$O$_3$−SiO$_2$. On the TiO$_2$ supported catalysts, it was possible to identify the rutile and anatase crystalline phases together with metallic Cu with an fcc structure. The analysis of the size of CuO and Cu crystalline domains using the Debye−Scherrer model (eq 4) showed important differences between the different catalysts (see Table S7). Initially, the oxidized catalysts had average crystallite sizes of CuO ranging from 27 to 40 nm. Upon reduction at 300 °C in H$_2$, the crystallite size increased significantly in all the catalysts, except on SiO$_2$−Al$_2$O$_3$. Under reduced environments at high temperature, catalyst sintering is accelerated, which leads to particle growth. The process is strongly related to the initial dispersion of the metals,[82−84] the Cu precursor,[85] the presence of additives,[86] metal−support interaction,[54] reduction temperature,[87] and spatial distribution of the metal clusters.[71] Therefore, it is possible that the drastic particle growth observed during reduction observed on Cu/SiO$_2$ was caused by the relatively weak interaction of Cu-SiO$_2$ support. In contrast, the stronger metal support interactions of Cu with TiO$_2$ and Al$_2$O$_3$−SiO$_2$ led to a lower sintering rate.[74,88] The average crystallite size showed significant deviation when compared to the HRTEM data. While it is true that crystallite size and particle sizes are not necessarily equal, the discrepancies herein observed could be due to the limitations of the HRTEM to capture large Cu clusters. In turn, the particle size distribution was artificially shifted to smaller sizes.

The results herein presented indicate that the activity, selectivity, and stability of the different catalysts during the methanol reforming reaction are strongly influenced by the acidity of the support, textural properties of the support, metal−support affinity, and to lesser extent the metal dispersion. In the case of Cu/SiO$_2$, the high surface area and moderate acidity seemed to result in high catalytic activity in terms of mass of the catalyst and high selectivity to H$_2$ even after long periods of time on stream (5−80 h).

4. CONCLUSIONS

A detailed study of methanol steam reforming reaction Cu catalyst supported on different metal oxides was performed to establish structure−activity relationships. This was accomplished by combining steam reforming experiments under different reaction conditions using Cu catalyst supported on nanosized SiO$_2$, Al$_2$O$_3$−SiO$_2$, TiO$_2$ rutile, and TiO$_2$ anatase. The results indicate that on highly acidic supports (e.g., Al$_2$O$_3$−SiO$_2$) the conversion of methanol rapidly decreased with the TOS. Thermal gravimetric analysis of the spent catalyst indicated the presence of carbon deposits, which could be responsible for the fast rates of deactivation. On TiO$_2$ anatase, the catalytic activity and stability were significantly lower than that obtained on homologous TiO$_2$ rutile. This observation was tentatively attributed to the differences in adsorbate−surface binding on TiO$_2$ rutile and anatase. Cu supported on nanosized SiO$_2$ showed the highest catalytic activity and selectivity among the materials screened. Steady state operation of Cu/SiO$_2$ catalyst was performed for over 80 h of reaction at low and high pressures and temperatures with no changes in activity and selectivity. However, metal sintering was observed after reaction by means of HRTEM and XRD. This deactivation was most likely masked by the high level of methanol conversion (∼80%). The high activity and selectivity of Cu/SiO$_2$ were attributed to the low acid site concentration. Notably, Cu supported on TiO$_2$ rutile showed very high activity and stability (771 μmol H$_2$·min^{-1}·g$_{cat}$$^{-1}$), which is rather unexpected for a catalyst with rather low specific surface area (10 m^2 g^{-1}).

■ ASSOCIATED CONTENT

Ⓢ Supporting Information

The Supporting Information is available free of charge on the ACS Publications website at DOI: 10.1021/acs.iecr.8b02488.

Additional details on the following results of catalyst characterization for the different catalysts herein employed, including peak distribution for the temperature-programmed reduction, deconvolution of the temperature-programmed desorption of NH_3, N_2-desorption isotherms, H_2 consumption, extent of CuO reduction, carbon deposits from thermal gravimetric analysis, and crystallite size; some supplementary results related to the catalytic activity, including product distribution as a function of time on stream (TOS) for Cu/SiO_2, hydrogen productivity as a function of the catalyst to feed ratio for the Cu/SiO_2 catalyst, Weisz–Prater criterion obtained for the different catalysts utilized for the reaction experiments, conversion, activity and selectivity for the different catalysts, conversion and product distribution as a function of temperature on Cu/SiO_2 (PDF)

■ AUTHOR INFORMATION

Corresponding Author

*Telephone: +31 534 89 71 15. E-mail: j.a.fariaalbanese@utwente.nl.

ORCID ⓘ

Juan Carlos Serrano-Ruiz: https://orcid.org/0000-0002-9078-7390

Jimmy Faria: 0000-0002-8920-3538

Notes

The authors declare no competing financial interest.

■ ACKNOWLEDGMENTS

■ REFERENCES

(1) Haryanto, A.; Fernando, S.; Murali, N.; Adhikari, S. Current Status of Hydrogen Production Techniques by Steam Reforming of Ethanol: A Review. *Energy Fuels* **2005**, *19* (19), 2098−2106.

(2) Ratnasamy, C.; Wagner, J. P. Water Gas Shift Catalysis. *Catal. Rev.: Sci. Eng.* **2009**, *51* (3), 325−440.

(3) Palo, D. R.; Dagle, R. A.; Holladay, J. D. Methanol Steam Reforming for Hydrogen Production. *Chem. Rev.* **2007**, *107* (107), 3992−4021.

(4) Sá, S.; Silva, H.; Brandão, L.; Sousa, J. M.; Mendes, A. Catalysts for methanol steam reforming — A review. *Appl. Catal., B* **2010**, *99*, 43−57.

(5) Yong-feng, L.; Xin-fa, D.; Wei-ming, L. Effects of ZrO2-promoter on catalytic performance of CuZnAlO catalysts for production of hydrogen by steam reforming of methanol. *Int. J. Hydrogen Energy* **2004**, *29*, 1617−1621.

(6) Liu, Y.; Hayakawa, T.; Suzuki, K.; Hamakawa, S.; et al. Highly active copper/ceria catalysts for steam reforming of methanol. *Appl. Catal., A* **2002**, *223*, 137−145.

(7) Peppley, B. A.; Amphlett, J. C.; Kearns, L. M.; Mann, R. F. Methanol-Steam Reforming on Cu/ZnO/Al2O3. Part 1: the reaction network. *Appl. Catal., A* **1999**, *179*, 21−29.

(8) Peppley, B. A.; Amphlett, J. C.; Kearns, L. M.; Mann, R. F. Methanol-Steam Reforming on Cu/ZnO/Al2O3. Part 2. A comprehensive kinetic model. *Appl. Catal., A* **1999**, *179*, 31−49.

(9) Lee, J. K.; Ko, J. B.; Kim, D. H. Methanol steam reforming over Cu/ZnO/Al2O3 catalyst: kinetics and effectiveness factor. *Appl. Catal., A* **2004**, *278*, 25−35.

(10) Agrell, J.; Birgersson, H.; Boutonnet, M. Steam reforming of methanol over a Cu/ZnO/Al 2O3 catalyst: a kinetic analysis and strategies for suppression of CO formation. *J. Power Sources* **2002**, *106*, 249−257.

(11) Matsumura, Y.; Ishibe, H. High temperature steam reforming of methanol over Cu/ZnO/ZrO2 catalysts. *Appl. Catal., B* **2009**, *91*, 524−532.

(12) Jiang, C. J.; Trimm, D. L.; Wainwright, M. S.; Cant, N. W. Kinetic study of steam reforming of methanol over copper-based catalysts. *Appl. Catal., A* **1993**, *93*, 245−255.

(13) Takezawa, N.; Iwasa, N. Steam reforming and dehydrogenation of methanol: Difference in the catalytic functions of copper and group VIII metals. *Catal. Today* **1997**, *36*, 45−56.

(14) Kniep, B. L.; Ressler, T.; Rabis, A.; Girgsdies, F.; Baenitz, M.; Steglich, F.; Schlogl, R. Rational Design of Nanostructured Copper−Zinc Oxide Catalysts for the Steam Reforming of Methanol. *Angew. Chem., Int. Ed.* **2004**, *43*, 112−115.

(15) Agrell, J.; Birgersson, H.; Boutonnet, M.; Melián-cabrera, I.; Navarro, R. M.; Fierro, J. L. G.; et al. Production of hydrogen from methanol over Cu/ZnO catalysts promoted by ZrO2 and Al2O3. *J. Catal.* **2003**, *219*, 389−403.

(16) Shishido, T.; Yamamoto, Y.; Morioka, H.; Takaki, K.; Takehira, K. Active Cu/ZnO and Cu/ZnO/Al2O3 catalysts prepared by homogeneous precipitation method in steam reforming of methanol. *Appl. Catal., A* **2004**, *263*, 249−253.

(17) Jakdetchai, O.; Takayama, N.; Nakajima, T. Activity Enhancement of CuZn-impregnated FSM-16 by Modification with 1,3-Butanediol for Steam Reforming of Methanol. *Kinet. Catal.* **2005**, *46* (1), 56−64.

(18) Jones, S. D.; Hagelin-weaver, H. E. Steam reforming of methanol over CeO2- and ZrO2-promoted Cu-ZnO catalysts supported on nanoparticle Al2O3. *Appl. Catal., B* **2009**, *90*, 195−204.

(19) Patel, S.; Pant, K. K. Selective production of hydrogen via oxidative steam reforming of methanol using Cu−Zn−Ce−Al oxide catalysts. *Chem. Eng. Sci.* **2007**, *62*, 5436−5443.

(20) Yang, S.; He, J.; Zhang, N.; Sui, X.; Zhang, L.; Yang, Z. Effect of rare-earth element modification on the performance of Cu/ZnAl catalysts derived from hydrotalcite precursor in methanol steam reforming. *J. Fuel Chem. Technol.* **2018**, *46* (2), 179−188.

(21) Tajrishi, O. Z.; Taghizadeh, M.; Kiadehi, A. D. Methanol steam reforming in a microchannel reactor by Zn-, Ce- and Zr- modified mesoporous Cu/SBA-15 nanocatalyst. *Int. J. Hydrogen Energy* **2018**, *43*, 14103−14120.

(22) Sanches, S. G.; Flores, J. H.; da Silva, M. I. P. Cu/ZnO and Cu/ZnO/ZrO2 catalysts used for methanol steam reforming. *Mol. Catal.* **2018**, *454*, 55−62.

(23) Ajamein, H.; Haghighi, M.; Alaei, S. The role of various fuels on microwave-enhanced combustion synthesis of CuO/ZnO/Al2O3 nanocatalyst used in hydrogen production via methanol steam reforming. *Energy Convers. Manage.* **2017**, *137*, 61−73.

(24) Bagherzadeh, S. B.; Haghighi, M. Plasma-enhanced comparative hydrothermal and coprecipitation preparation of CuO/ZnO/Al2O3 nanocatalyst used in hydrogen production via methanol steam reforming. *Energy Convers. Manage.* **2017**, *142*, 452−465.

(25) Liu, X.; Toyir, J.; Ramirez de la Piscina, P.; Homs, N. Hydrogen production from methanol steam reforming over Al2O3- and ZrO2-modified. *Int. J. Hydrogen Energy* **2017**, *42*, 13704−13711.

(26) Takezawa, N.; Kobayashi, H.; Hirose, A.; Shimokawabe, M.; Takahashi, K. Steam reforming of methanol on copper-silica catalysts; effect of copper loading and calcination temperature on the reaction. *Appl. Catal.* **1982**, *4*, 127−134.

(27) Shishido, T.; Yamamoto, Y.; Morioka, H.; Takehira, K. Production of hydrogen from methanol over Cu/ZnO and Cu/

ZnO/Al2O3 catalysts prepared by homogeneous precipitation: Steam reforming and oxidative steam reforming. *J. Mol. Catal. A: Chem.* **2007**, *268*, 185−194.

(28) Matter, P. H.; Braden, D. J.; Ozkan, U. S. Steam reforming of methanol to H2 over nonreduced Zr-containing CuO/ZnO catalysts. *J. Catal.* **2004**, *223*, 340−351.

(29) Yi, N.; Si, R.; Saltsburg, H.; Flytzani-stephanopoulos, M. Steam reforming of methanol over ceria and gold-ceria nanoshapes. *Appl. Catal., B* **2010**, *95*, 87−92.

(30) Su, T.-B.; Rei, M.-H. Steam Reforming of Methanol over Nickel and Copper Catalysts. *J. Chin. Chem. Soc.* **1991**, *38* (6), 535−541.

(31) Huang, Y.; Wang, S.; Tsai, A.; Kameoka, S. Reduction behaviors and catalytic properties for methanol steam reforming of Cu-based spinel compounds CuX 2 O 4 (X = Fe, Mn, Al, La). *Ceram. Int.* **2014**, *40*, 4541−4551.

(32) Lebarbier, V.; Dagle, R.; Conant, T.; Vohs, J. M.; Datye, A. K.; Wang, Y. CO/FTIR Spectroscopic Characterization of Pd/ZnO/Al2O3 Catalysts for Methanol Steam Reforming. *Catal. Lett.* **2008**, *122*, 223−227.

(33) Oguchi, H.; Nishiguchi, T.; Matsumoto, T.; Kanai, H.; Utani, K.; Matsumura, Y.; Imamura, S. Steam reforming of methanol over Cu/CeO2/ZrO2 catalysts. *Appl. Catal., A* **2005**, *281*, 69−73.

(34) Tsai, M.; Wang, J.; Shen, C.; Yeh, C. Promotion of a copper−zinc catalyst with rare earth for the steam reforming of methanol at low temperatures. *J. Catal.* **2011**, *279*, 241−245.

(35) Kim, S.; Kang, M. Hydrogen production from methanol steam reforming over Cu-Ti-P oxide catalysts. *J. Ind. Eng. Chem.* **2012**, *18* (3), 969−978.

(36) Pongstabodee, S.; Monyanon, S.; Luengnaruemitchai, A. Hydrogen production via methanol steam reforming over Au/CuO, Au/CeO 2, and Au/CuO-CeO 2 catalysts prepared by deposition-precipitation. *J. Ind. Eng. Chem.* **2012**, *18* (4), 1272−1279.

(37) Tahay, P.; Khani, Y.; Jabari, M.; Bahadoran, F.; Safari, N. General Highly porous monolith/TiO2 supported Cu, Cu-Ni, Ru, and Pt catalysts in methanol steam reforming process for H2 generation. *Appl. Catal., A* **2018**, *554*, 44−53.

(38) Taghizadeh, M.; Akhoundzadeh, H.; Rezayan, A.; Sadeghian, M. Excellent catalytic performance of 3D-mesoporous KIT-6 supported Cu and Ce nanoparticles in methanol steam reforming. *Int. J. Hydrogen Energy* **2018**, *43*, 10926−10937.

(39) Phongboonchoo, Y.; Thouchprasitchai, N.; Pongstabodee, S. Hydrogen production with a low carbon monoxide content via methanol steam reforming over CuxCeyMgz/Al2O3 catalysts: Optimization and stability. *Int. J. Hydrogen Energy* **2017**, *42*, 12220−12235.

(40) Jampa, S.; Jamieson, A. M.; Chaisuwan, T.; Luengnaruemitchai, A.; Wongkasemjit, S. Achievement of hydrogen production from autothermal steam reforming of methanol over Cu-loaded mesoporous CeO2 and Cu-loaded mesoporous CeO2 ZrO2 catalysts. *Int. J. Hydrogen Energy* **2017**, *42*, 15073−15084.

(41) Lunkenbein, T.; Girgsdies, F.; Kandemir, T.; Thomas, N.; Behrens, M.; Schlögl, R.; Frei, E. Bridging the Time Gap: A Copper/Zinc Oxide/Aluminum Oxide Catalyst for Methanol Synthesis Studied under Industrially Relevant Conditions and Time Scales. *Angew. Chem., Int. Ed.* **2016**, *55* (41), 12708−12712.

(42) Behrens, M.; Studt, F.; Kasatkin, I.; Kühl, S.; Hävecker, M.; Abild-pedersen, F.; Zander, S.; Girgsdies, F.; Kurr, P.; Kniep, B.; et al. The Active Site of Methanol Synthesis over Cu/ZnO/Al2O3 Industrial Catalysts. *Science (Washington, DC, U. S.)* **2012**, *336*, 893−898.

(43) Manzolini, G.; Jansen, D. Economic analysis of systems for electrical energy and hydrogen production: fundamentals and application to two membrane reactor processes. In *Handbook of Membrane Reactors: Vol. 2: Reactor Types and Industrial Applications*; Basile, A., Ed.; Woodhead Publishing Limited: Cambridge, 2013; pp 528−550.

(44) Santarelli, M.; Medina, P.; Calì, M. Fitting regression model and experimental validation for a high-pressure PEM electrolyzer. *Int. J. Hydrogen Energy* **2009**, *34*, 2519−2530.

(45) Marangio, F.; Santarelli, M.; Calì, M. Theoretical model and experimental analysis of a high pressure PEM water electrolyser for hydrogen production. *Int. J. Hydrogen Energy* **2009**, *34*, 1143−1158.

(46) Watson, B. A.; Barteau, M. A. Atomic Force Microscopy Imaging of TiO2 Surfaces Active for C-C Bond Formation Reactions in Ultrahigh Vacuum. *Chem. Mater.* **1994**, *6* (16), 771−779.

(47) Barteau, M. A. Organic Reactions at Well-Defined Oxide Surfaces. *Chem. Rev.* **1996**, *96*, 1413−1430.

(48) Rekoske, J. E.; Barteau, M. A. Isothermal Reduction Kinetics of Titanium Dioxide-Based Materials. *J. Phys. Chem. B* **1997**, *101* (7), 1113−1124.

(49) Bukhavtsova, N. M.; Ostrovskii, N. M. Catalytic reaction accompanied by capillary condensation. 3. Infuence on reaction kinetics and dynamics. *React. Kinet. Catal. Lett.* **1998**, *65* (2), 321−329.

(50) Singh, U. K.; Vannice, M. A. Kinetics of liquid-phase hydrogenation reactions over supported metal catalysts - a review. *Appl. Catal., A* **2001**, *213*, 1−24.

(51) Mukherjee, S.; Vannice, M. A. Solvent effects in liquid-phase reactions II. Kinetic modeling for citral hydrogenation. *J. Catal.* **2006**, *243* (1), 131−148.

(52) Madon, R. J.; O'Connell, J. P.; Boudart, M. Catalytic hydrogenation of cyclohexene: Part II. Liquid phase reaction on supported platinum in a gradientless slurry reactor. *AIChE J.* **1978**, *24* (5), 904−911.

(53) Madon, R. J.; Iglesia, E. Catalytic reaction rates in thermodynamically non-ideal systems. *J. Mol. Catal. A: Chem.* **2000**, *163* (1−2), 189−204.

(54) Haller, G. L.; Resasco, D. E. Metal-Support Interaction: Group Vlll Metals and Reducible Oxides. *Adv. Catal.* **1989**, *36*, 173−235.

(55) Che, M.; Bennett, C. The Influence of Particle Size on the Catalytic Properties of Supported Metals. *Adv. Catal.* **1989**, *36*, 55−172.

(56) Hicks, R. F.; Fleisch, T. H.; Bell, A. T. An XPS Study of Metal-Support Interactions on Pd/SiO2 and Pd/La2O3. *J. Catal.* **1984**, *87*, 398−413.

(57) Sagar, G. V.; Rao, R.; Srikanth, C. S.; Chary, K. V. R. Dispersion and Reactivity of Copper Catalysts Supported on Al2O3-ZrO2. *J. Phys. Chem. B* **2006**, *110*, 13881−13888.

(58) Zhao, E. W.; Zheng, H.; Ludden, K.; Xin, Y.; Hagelin-Weaver, H. E.; Bowers, C. R. Strong Metal-Support Interactions Enhance the Pairwise Selectivity of Parahydrogen Addition over Ir/TiO2. *ACS Catal.* **2016**, *6*, 974−978.

(59) Demmin, R. A.; Gorte, R. J. Design Parameters for Temperature-Programmed from a Packed Bed. *J. Catal.* **1984**, *90*, 32−39.

(60) Gorte, R. J. Temperature-programmed desorption for the characterization oxide catalysts. *Catal. Today* **1996**, *28*, 405−414.

(61) Kouva, S.; Kanervo, J.; Schüßler, F.; Olindo, R.; Lercher, J. A.; Krause, O. Sorption and diffusion parameters from vacuum-TPD of ammonia on H-ZSM-5. *Chem. Eng. Sci.* **2013**, *89*, 40−48.

(62) Coppens, M. O. Characterization of fractal surface roughness and its influence on diffusion and reaction. *Colloids Surf., A* **2001**, *187−188*, 257−265.

(63) Aranda-Pérez, N.; Ruiz, M. P.; Echave, J.; Faria, J. Enhanced Activity and Stability of Ru-TiO2 Rutile for Liquid Phase Ketonization. *Appl. Catal., A* **2017**, *531*, 106−118.

(64) Pham, T. N.; Shi, D.; Sooknoi, T.; Resasco, D. E. Aqueous-phase ketonization of acetic acid over Ru/TiO2/carbon catalysts. *J. Catal.* **2012**, *295*, 169−178.

(65) Mapes, J. E.; Eischens, R. P. TThe infrared spectra of ammonia chemisorbed on cracking catalysts. *J. Phys. Chem.* **1954**, *58*, 1059−1062.

(66) Milliken, T. H. J.; Mills, G. A.; Oblad, A. G. The chemical characteristics and structure of cracking catalysts. *Discuss. Faraday Soc.* **1950**, *8*, 279−290.

(67) Huang, X.; Cant, N. W.; Wainwright, M. S.; Ma, L. The dehydrogenation of methanol to methyl formate Part I: Kinetic

studies using copper-based catalysts. *Chem. Eng. Process.* **2005**, *44*, 393−402.

(68) Yarulina, I.; Chowdhury, A. D.; Meirer, F.; Weckhuysen, B. M.; Gascon, J. Recent trends and fundamental insights in the methanol-to-hydrocarbons process. *Nat. Catal.* **2018**, *1* (6), 398−411.

(69) Wu, D.; Song, L.; Zhang, B.; Li, Y. Effect of the mechanical failure of catalyst pellets on the pressure drop of a reactor. *Chem. Eng. Sci.* **2003**, *58*, 3995−4004.

(70) Zhang, L.; Chen, K.; Chen, B.; White, J. L.; Resasco, D. E. Factors that Determine Zeolite Stability in Hot Liquid Water. *J. Am. Chem. Soc.* **2015**, *137* (36), 11810−11819.

(71) Prieto, G.; Zečević, J.; Friedrich, H.; de Jong, K. P.; de Jongh, P. E. Towards stable catalysts by controlling collective properties of supported metal nanoparticles. *Nat. Mater.* **2013**, *12* (1), 34−39.

(72) Asprey, S. P.; Wojciechowski, B. W.; Peppley, B. A. Kinetic studies using temperature-scanning: the steam-reforming of methanol. *Appl. Catal., A* **1999**, *179*, 51−70.

(73) Robbins, J. L.; Kelkar, C. P.; Iglesia, E.; DeRites, B. Methanol synthesis over C u/SiO2 catalysts. *Catal. Lett.* **1991**, *10*, 1−10.

(74) Liu, Y.; Hayakawa, T.; Tsunoda, T.; Suzuki, K.; Hamakawa, S.; Murata, K.; Shiozaki, R.; Ishii, T.; Kumagai, M. Steam reforming of methanol over Cu/CeO2 catalysts studied in comparison with Cu/ZnO and Cu/Zn(Al)O catalysts. *Top. Catal.* **2003**, *22* (3−4), 205−213.

(75) Adams, C. R.; Benesi, H. A.; Meisenheimer, R. G. Particle Size Determination of Supported Catalytic Materials: Platinum on Silica Gel. *J. Catal.* **1962**, *1*, 336−344.

(76) Harris, P. Growth and Structure of Supported Metal Catalyst Particles. *Int. Mater. Rev.* **1995**, *40* (3), 97−115.

(77) Meghana, S.; Kabra, P.; Chakraborty, S.; Padmavathy, N. Understanding the pathway of antibacterial activity of copper oxide nanoparticles. *RSC Adv.* **2015**, *5*, 12293−12299.

(78) Kayani, Z. N.; Umer, M.; Riaz, S.; Naseem, S. Characterization of Copper Oxide Nanoparticles Fabricated by the Sol-Gel Method. *J. Electron. Mater.* **2015**, *44* (10), 3704−3709.

(79) Jensen, H.; Pedersen, J. H.; Jørgensen, J. E.; Pedersen, J. S.; Joensen, K. D.; Iversen, S. B.; Søgaard, E. G. Determination of size distributions in nanosized powders by TEM, XRD, and SAXS. *J. Exp. Nanosci.* **2006**, *1* (3), 355−373.

(80) Yan, J.; Wu, G.; Guan, N.; Li, L.; Li, Z.; Cao, X. Understanding the effect of surface/bulk defects on the photocatalytic activity of TiO2: anatase versus rutile. *Phys. Chem. Chem. Phys.* **2013**, *15*, 10978−10988.

(81) Dung Dang, T. M.; Tuyet Le, T. T.; Fribourg-Blanc, E.; Chien Dang, M. The influence of solvents and surfactants on the preparation of copper nanoparticles by a chemical reduction method. *Adv. Nat. Sci.: Nanosci. Nanotechnol.* **2011**, *2* (2), 025004.

(82) Kim, W.; Mohaideen, K. K.; Seo, D. J.; Yoon, W. L. Methanol-steam reforming reaction over Cu-Al-based catalysts derived from layered double hydroxides. *Int. J. Hydrogen Energy* **2017**, *42*, 2081−2087.

(83) Azenha, C. S. R.; Mateos-pedrero, C.; Queirós, S.; Concepción, P.; Mendes, A. Environmental Innovative ZrO2-supported CuPd catalysts for the selective production of hydrogen from methanol steam reforming. *Appl. Catal., B* **2017**, *203*, 400−407.

(84) Gates, B. C. Supported Metal Clusters: Synthesis, Structure, and Catalysis. *Chem. Rev.* **1995**, *95*, 511−522.

(85) Qin, F.; Liu, Y.; Qing, S.; Hou, X.; Gao, Z. Cu-Al spinel as a sustained release catalyst for H2 production from methanol steam reforming: Effects of different copper sources. *J. Fuel Chem. Technol.* **2017**, *45* (12), 1481−1488.

(86) Lei, Y.; Luo, Y.; Li, X.; Lu, J.; Mei, Z.; Peng, W.; Chen, R.; Chen, K.; Chen, D.; He, D. The role of samarium on Cu/Al2O3 catalyst in the methanol steam reforming for hydrogen production. *Catal. Today* **2018**, *307*, 162−168.

(87) Coq, B.; Dutartre, R.; Figueras, F.; Tazi, T. Particle Size, Precursor, and Support Effects in the Hydrogenolysis of Alkanes Over Supported Rhodium Catalysts. *J. Catal.* **1990**, *122*, 438−447.

(88) Mrad, M.; Gennequin, C.; Aboukaïs, A.; Abi-aad, E. Cu/Zn-based catalysts for H2 production via steam reforming of methanol. *Catal. Today* **2011**, *176*, 88−92.